Structure, Nanomechanics, and Dynamics of Dispersed Surfactant-Free Clay Nanocomposite Films

Xiao Zhang,[1] Jing Zhao,[1,2] Chad R. Snyder ![ORCID],[2] Abdullah Al-Enizi,[3] Ahmed Eltazahry,[4] David S. Simmons ![ORCID],[1] Alamgir Karim ![ORCID][1]*

[1]Department of Polymer Engineering, University of Akron, Akron, Ohio, 44325
[2]Materials Science and Engineering Division, National Institute of Standards and Technology, Gaithersburg, Maryland, 20899
[3]Chemistry Department, Faculty of Science, King Saud University, Riyadh, 11451, Saudi Arabia
[4]Materials Science and Technology Program, College of Arts and Sciences, Qatar University, PO Box 2713, Doha, Qatar & Polymer Materials Research Department, Advanced Technology and New Materials Research Institute, City for Scientific Research and Technology Applications, New Borg El-Arab City, Alexandria, Egypt

The current work presents a new approach to achieve high quality dispersion of surfactant-free nanoclay tactoid particles in sub-micron thin films despite the absence of organic modifier. Natural Montmorillonite particles, Na$^+$ Cloisite, were dispersed in thin films of polycaprolactone (PCL) through a flow coating technique assisted by ultrasonication. Wide-angle X-ray scattering (WAXS), grazing-incidence wide-angle X-ray scattering (GI-WAXS), and transmission electron microscopy (TEM) were used to confirm the level of natural clay dispersion down to the level of tactoids (sub-micron scale stacks of clay sheets). These characterization techniques were carried out in conjunction with an analysis of nanomechanical properties via strain-induced buckling instability for modulus measurements (SIEBIMM), a high-throughput technique to characterize thin film mechanical properties. The buckling patterns indicate that the natural clay tactoids separate buckling-enhancing (high-modulus) crystalline regions and interconnect buckling-suppressing amorphous (low-modulus) regions. Due to the tactoid length scale, the glass transition behavior of the composites as characterized by broadband dielectric relaxation spectroscopy was unmodified by the clay. Likewise, the glass transition temperature, T_g, and fragility (slope of relaxation time behavior approaching T_g), remain unaffected, indicating that these dispersed tactoids do not induce pronounced confinement effects on dynamics. POLYM. ENG. SCI., 58:1285–1295, 2018. © 2018 Society of Plastics Engineers

INTRODUCTION

Polymer/clay nanocomposites (PCN) have been widely investigated in recent decades towards preparation methods and determining the associated improvements in a broad range of applications [1]. Common strategies to obtain nanocomposite morphologies involve but are not limited to one or a combination of the following routes: adding polar functional groups through reactive melt processing [2–5], using quaternary ammonium salts as coupling agents [6–8], in-situ polymerization, [9–12], latex coagulation [13–15], and layer-by-layer (LBL) assembly of polyelectrolytes [16–19]. The majority of the relevant literature nowadays tends to exhibit a ubiquitous understanding that a promising level of intercalation and exfoliation can be achieved with attractive polymer-clay interactions, whereas microcomposite-like aggregation is broadly observed with weak associations between clay galleries and molecular chains. All of these attractive polymer-clay interaction-based strategies involve incorporating surfactants within the clay galleries. This well-accepted phenomenon, while bringing meaningful insights to various processing techniques, needs to be further explored to develop better correlations between dispersion morphologies and surface interactions. Understanding the peculiarity of well-dispersed systems with weak polymer-nanoparticle interactions seems thus beneficial for the development of novel additives for polymeric materials. From a more practical standpoint, it is more economical and desirable from a "green" perspective to develop a surfactant-free approach for a new class of nanocomposites with intermediate properties. From a more practical standpoint, it is more economical and desirable from a "green" perspective to develop a surfactant free approach for a new class of nanocomposites with intermediate properties. Our study briefly illustrates the surfactant-free approach to nanocomposites formulation, but significant development of this approach is required for substantial property enhancements. We hope our work inspires future studies in this direction.

Mackay et al. have previously demonstrated that nanoparticle dispersion can be achieved with the absence of strong surface interactions and structural similarities through rapid precipitation from the solution with enlarged difference between the particle size and radius of gyration [20]. Guinier analysis of Small Angle Neutron Scattering (SANS) and microscopy studies have proven that branched dendritic polyethylene nanoparticles can exist in polystyrene matrix in a highly dispersed state and effectively modify the host matrix radius of gyration despite the evident incompatibility between the two systems [21, 22]. Similarly, ligand-free quantum dots and fullerene nanoparticles have been dispersed in polystyrene with particle sizes smaller than the Edward's tube radius, leading to a deviation from the Stokes-Einstein relation and an unusual decrease in polymer melt viscosity [23, 24]. Therefore, the application of a comparable approach can be extended to polymer–clay systems. To our knowledge, virtually no detailed experimental efforts have focused on the effect of well-dispersed nanoclay on the performance of the host matrix

without strong surface interactions. In this work, we present a new methodology to achieve high quality dispersion of surfactant-free nanoclay particles in polycaprolactone (PCL) matrix regardless of their dissimilar chemical structures and the absence of organic modifier. Polycaprolactone (PCL), as a type-A polymer having a molecular dipole perpendicular to the chain axis and relatively flexible backbone, is suitable for this type of study. Inherently, the moderate backbone flexibility enables molecular chains to easily diffuse and allows polar carbonyl groups to engage in weak hydrogen bonding interactions with the hydroxyl groups intrinsically embedded inside the layered silicates. A variety of studies suggest that colloidal suspension of clay minerals in water can invoke the swelling of the galleries as water molecules inside the inter-gallery spacing are able to weaken the electrostatic tractions among the charged layers [25]. Hence, intense stirring and ultrasonication can effectively lower the particle size or even exfoliate the silicate layers. As such, pre-dispersing natural clay particles in an aqueous media, known as water-assisted compounding, is effective in many water soluble systems [26–29]. However, it remains uncertain how specific dispersion morphologies, such as geometry and particle size distribution, are related to the overall properties with the absence of organic surfactant.

Building upon previous studies of polymer–clay nanocomposites and nanoparticle dispersion tactics, the current research combines the advantages of water-assisted compounding and Mackay's proposed method [20], as described previously. In essence, a small amount of ultrasound treated water clay mixture is introduced to the PCL solution while undergoing intense probe sonication. The resultant liquid mixture in the form of colloidal suspension is immediately cast into submicron thin films through flow coating, a well-known technique to fabricate substrate supported ultrathin films with desired thickness gradient [30]. Due to the hydrophilic nature of natural clay particles, Mackay's method by itself poses a risk of losing clay particles into alcohol-based solvents during the precipitation step. Alternatively, the same outcome of rapid coagulation can be achieved through flow coating without precipitation of polymer with clay-dissolving non-solvents, and as a result, an accurate amount of clay loading can be safely maintained. In the current work, this combined technique turns out to be effective to prepare highly dispersed PCL/natural clay nanocomposite thin films. Despite a slower solvent evaporation rate, freestanding bulk films produced through drop casting also exhibit the characteristics of nanocomposites. The well-dispersed tactoid-like morphologies of the resultant composites were examined and confirmed by transmission electron microscopy (TEM), wide angle X-ray scattering (WAXS), and grazing-incidence wide angle X-ray scattering (GIWAXS).

The foremost aspect of nanoparticle effects on the polymer matrix lies in mechanical property changes, commonly delineated by strengthened or weakened elastic modulus. In nanocomposite systems, a small fraction of fillers can cause evident increases in elastic modulus. Contrary to nanocomposites, micro-composites often exhibit decreased elastic modulus when the filler concentration is low. Composite samples in the form of substrate-supported ultrathin film with uniform thickness allow us to link dispersion morphologies with mechanical properties. Indeed, the high quality of thickness uniformity achieved through flow coating allows a promising resolution to conduct microscopy analysis, especially for well-dispersed nanocomposite systems [31]. At the same time, the associated variation in mechanical performance is assessable through strain-induced elastic buckling instability for mechanical measurements (SIEBIMM), a high throughput metrology to manifest thin film mechanical properties. In this technique, the film is transferred to an elastomeric substrate, which, subsequently, undergoes uniaxial elongation to produce a periodical buckling pattern of the thin film [32, 33]. SIEBIMM has been broadly applied to many polymer systems due to the growing interests in submicron thin film mechanical properties [34–38]. An example comes from a relevant study on polymer-clay systems, specifically organoclay-filled PCL and PLA biopolymers, which showed that intercalated layered silicates in the presence of organic modifiers are effective to increase the elastic modulus of the polymer matrix [39].

Here, we attempt to investigate the influence of well-dispersed natural clay in the same matrix and relate the relevant property changes to the nanoscale morphologies. Furthermore, for a periodic buckling pattern to occur, the thin film of interest needs to be significantly stiffer than the soft substrate. Therefore, it is preferable to perform the experiment below its T_g. PCL is a semi-crystalline polymer consisting of a rigid crystalline domain and a soft amorphous domain with a around 213K. Because room temperature is significantly higher than PCL's T_g, buckling is enhanced in the crystalline domain and suppressed in the amorphous domain, resulting in buckling-rich regimes and buckling-deficient regimes on the obtained images. In this study, we have analyzed both regimes in detail and found that natural clay tactoids prefer to remain in the buckling-deficient (amorphous) regions. Understandably, in the absence of organophilic surfactants, natural clay tactoids are more likely to engage in weak hydrogen bonding with the more flexible amorphous phase rather than with the stiff crystalline phase.

In nanoparticle systems, the interfacial confinement effect can result in property changes. Indeed, it has been suggested that nanocomposites are analogous to ultrathin films confined by the interfaces near the substrate and atmosphere [40, 41]. Shifts in T_g due to "interfacial confinement" in these systems have been shown to result from a gradient in dynamics in the direction perpendicular to the interface [42–44]. In essence, segmental dynamics near the interface are altered while segments far away from the interface are less affected [45–49]. Moreover, these effects depend on the strength of interfacial interactions. Strong attractive interactions favor an increase in T_g and slower segmental dynamics near the matrix-particle interface, whereas non-attractive interactions favor a reduced T_g and faster dynamics [42, 50]. Intermediate interaction strengths can yield a "compensation effect" wherein bulk-like dynamics are recovered [50, 51].

We investigate the glass transition behavior of the bulk nanocomposite films in a thickness range around 50 μm. Two types of interfacial confinement effect can be anticipated. First, it has long been known that interfacial interactions between amorphous and crystalline domains in semicrystalline polymers can induce the formation of a "rigid amorphous fraction" of amorphous material with suppressed dynamics [52]. Simulation results indicate that this effect is likely physically equivalent to alterations in dynamics near nanoparticles and in thin films [53]. Second, as discussed above the nanofillers can also induce spatially varying alterations in dynamics. Previous studies on PCL-organoclay systems using dielectric spectroscopy have not identified major changes in chain dynamics during in this particular polymer/nanoparticle pair in typical loading ranges [54]. Here,

we conduct a comparative study on the effect of natural clay tactoids.

In this paper, TEM images and related digital analysis summarize the overall uniformity of natural clay dispersion and specific geometric aspects, such as particle size distribution and aspect ratio. These dispersion morphologies are further corroborated by wide angle X-ray scattering (WAXS) and grazing-incidence wide angle X-ray scattering (GIWAXS) results. In addition, regional mechanical properties were characterized using SIEBIMM. The buckling patterns associated with dispersion morphologies and crystallinity have been discussed. Aspect ratio, an important parameter obtained in Halpin-Tsai (HT) fitting, is compared with the results of TEM image analysis. Finally, we investigate dynamic properties, such as fragility, and -relaxation activation energy using dielectric spectroscopy. Results have been compared with earlier studies on PCL-organoclay systems.

EXPERIMENTAL PROCEDURE

Materials

Poly (ε-caprolactone) with a number-average relative molar mass of ≈ 80,000 g/mol, was obtained from Sigma-Aldrich [48]. Laboratory grade toluene, purchased from BDH chemicals, was used for preparing 2% mass fraction polymer solutions for flow coating and drop casting. All the materials were directly used without further purification. Sodium Cloisite (Na MMT), known as the highly refined Montmorillonite, has a cation-exchange capacity (CEC) of 92 mequiv/100 g. According to the product information, the average inter-gallery spacing is 11.7 Å, which is consistent with our WAXS results. Silicon wafers, purchased from Silicon Quest International, were used as substrates for flow coating and were treated with UV Ozone, generated by a Novascan UV chamber. Sylgard 182 Dow Corning Polydimethylsiloxane (PDMS) served as the elastomer substrate for the buckling measurements (SIEBIMM) and was prepared with a 20:1 elastomer base-crosslinker ratio. The mixture of base and curing agent was intensively stirred prior to the solidification by oven annealing at 120°C for 2 h.

Fabrication of Nanocomposites

1% mass fraction natural clay/water mixture was stirred with Fisher Scientific vortex for an hour and intensively treated with CAMLAB Transsonic probe ultra-sonication to ensure that the layered silicates were in a well-dispersed state before coming into contact with polymer solution. The resultant water–clay suspension liquid is introduced drop-wise into the polymer solution undergoing the same type of intense ultra-sonication. A calculated amount of water/clay mixture was introduced to each polymer solution to produce the desired polymer/clay weight fraction. Following the standard flow coating procedures reported in the literature [30], around 20 μL of the subsequent mixture is immediately deposited into the gap between the glass blade and silicon wafer. The flow coating velocity is controlled at 15 mm/s to produce thin films around 120 nm. Film thicknesses were measured from a F20-UV Interferometer supplied by Filmetrics. The prepared substrate-supported thin films were placed into a vacuum desiccator to remove the residual solvents. Similarly, the free standing thick films were drop-cast from the same liquid suspension system onto ultraviolet (UV)-Ozone

treated glass petri dishes and dried under room temperature for 1 h. The produced films were peeled off from the petri dishes and vacuum dried overnight.

Characterization

Flow coated thin films were carefully floated on water by emerging the silicon substrate into deionized water. The floated thin films were picked up by copper grids for microscopy analysis. JEM-1200XII transmission electron microscope (TEM) was used to visually characterize the dispersion morphology. Wide-angle X-ray diffraction (WAXD) measurements were carried out using a Bruker Discovery X-ray diffractometer with Cu-K$_\alpha$ radiation and a wavelength of ≈1.54 Å for the natural clay powder and freestanding thick films. GIWAXS was conducted at the Synchrotron Light Source at the Argonne National Lab with an incident X-ray beam with a wavelength of 1.6 Å for flow coated thin film samples. Differential Scanning Calorimetry (DSC) measurements were performed using a TA Q200 calorimeter. Each sample is heated up to 100°C and held isothermal for 2 min to erase thermal history, followed by cooling to −100°C with a constant cooling rate of 10°C/min. Melting peak integration was performed using TA Universal Analysis software to obtain crystallinity.

Mechanical Measurements

Strain-induced elastic buckling instability for mechanical measurements (SIEBIMM) was the key technique to characterize the elastic modulus changes of the composite thin film samples. Following the same steps from a previous study of PCL/Cloisite 30B systems [39], the flow-coated thin films supported by silicon substrate were transferred onto the PDMS substrate through the water immersion technique. During this procedure, the thin films were already fabricated and dried before transferring. Therefore, even though natural clay particles are hydrophilic by nature, we assume that the water immersion should not affect the dispersion morphologies of the composite films. The modulus of the PDMS substrate was measured using a TA XT Plus texture analyzer equipped with miniature tensile grips. To produce a periodical buckling pattern of the transferred thin films, ≈3% of deformation was applied using a Newport Universal Motion Controller, an automated device to keep the deformation rate constant. Grayscale buckling images were taken using an Olympus Scientific optical microscope with a magnification level corresponding to 110.63 nm/pixel. The obtained images were further analyzed using a Matlab program to perform a fast Fourier transform for the statistical analysis of the buckling wavelength. The thin film elastic modulus was calculated using the same expression proposed by Stafford et al., shown as follows [32]:

$$\frac{E_f}{\left(1-v_f^2\right)} = \frac{3E_s}{\left(1-v_s^2\right)} \left(\frac{d}{2\pi h}\right)^3 \tag{1}$$

Here, E_f is the modulus of the thin film, E_s is the elastic modulus of the substrate, while v_f and v_s are the Poisson ratio of the thin film and the substrate, respectively. The term d is the buckling wavelength; h is the film thickness.
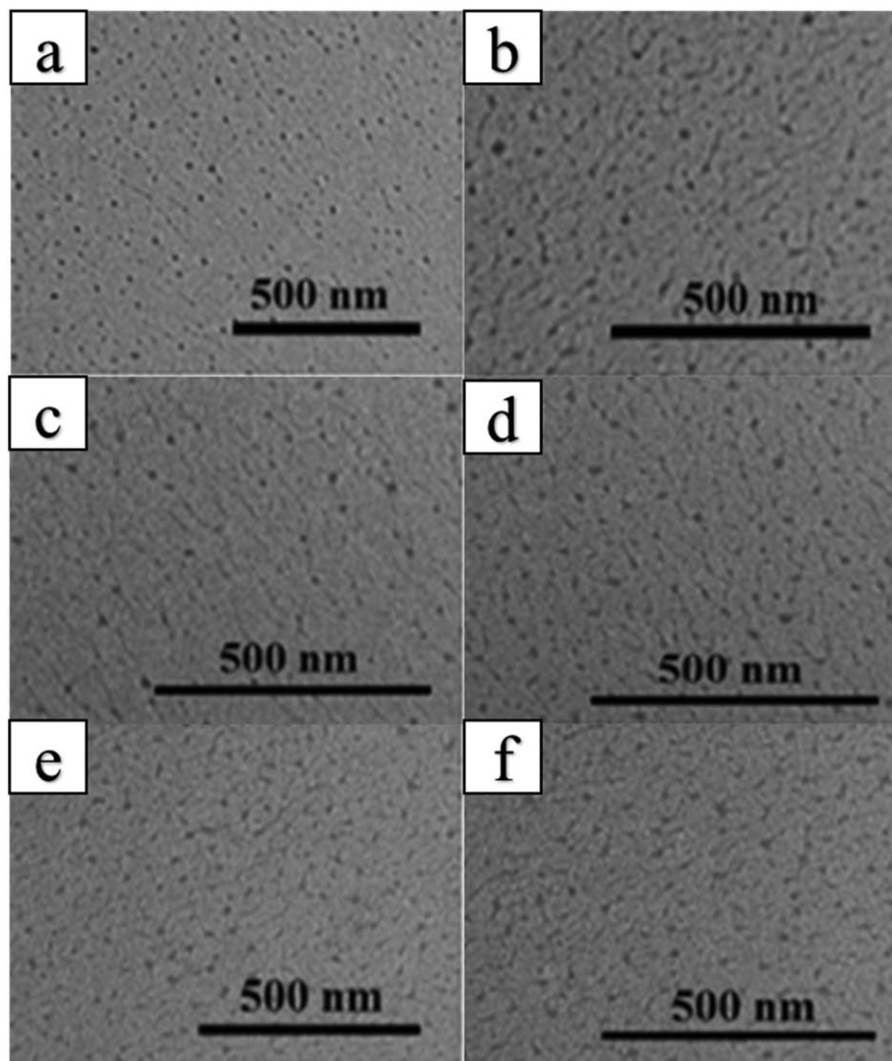
FIG. 1. TEM Images of PCL/Clay nanocomposites with 1% mass fraction Cloisite Na+ (a,b), 3% mass fraction Cloisite Na+ (c,d), and 5% mass fraction Cloisite Na+ (e,f). High quality dispersion can be confirmed by TEM images. Structured sheets of individual tactoids, represented by the dark lines and dots, are widely and homogeneously spread out. The high quality of dispersion is confirmed by the absence of huge clusters of dark areas.

Broadband Dielectric Spectroscopy

The bulk film obtained from drop-casting was put between cylindrical brass electrodes for a parallel plate geometry with ≈40 μm diameter silica spacers to control the thickness. The area of the sample was set by the smaller top brass electrode with diameter of 10 mm. The electrodes with the sample in between were put into the vacuum oven for 3 h before they were slowly cooled down to room temperature from 70°C. Concept 40 Novocontrol Alpha analyzer was used to performed the dielectric measurement with frequency range of 10^7 to 2.68×10^{-2} Hz. The temperature range of the test was (150 to −140)°C with a −5°C/step equilibrating at each temperature prior to dielectric measurements, and the sample temperature was controlled with a cooled or heated nitrogen purge.

RESULTS AND DISCUSSION

Thin films with highly uniform thicknesses were obtained using flow coating method, allowing a homogeneous electron density during the transmission electron microscopy (TEM) analysis. TEM images of samples with different clay contents (from 1% to 5% mass fraction) are shown in Fig. 1.

The thickness uniformity is verified by the identical color of the gray background representing the polymer matrix throughout the entire analyzed area, suggesting no electron density instabilities occurred due to the fluctuation in film thickness. Dark lines and dots represent the dispersed natural clay particles in the form of tactoids. The effectiveness of the proposed strategy is supported by the absence of huge clusters of dark areas. TEM micrographs are taken at two different locations for each clay concentration to confirm the stabilized dispersed nanostructure (Fig. 1). These tactoids, albeit somewhat connected in a tail-to-tail tadpole-like fashion, are generally well spread out, allowing digital analysis of detailed geometries. This tail-to-tail type of particle connection is observed for the polymer–clay system under TEM for the first time, indicating regional percolation of natural clay tactoids. TEM images of each composite sample were analyzed with

TABLE 1. Summary of TEM particle analysis.

Clay content mass fraction	Average size (nm^2)	Aspect ratio
1%	44.05 ± 44.34	2.38 ± 0.90
3%	41.34 ± 60.52	2.10 ± 1.18
5%	87.28 ± 99.79	2.06 ± 1.74

ImageJ. Particle size distribution was obtained by creating a color threshold of the analyzed image. The resulting mask images are shown in Fig. 3, with the remaining results tabulated in Table 1. The average size of the particles ranges from 40 to 80 nm^2, which is slightly aberrant from the particle size distribution curve (Fig. 2), displaying that the majority of the frequency peaks appear near 40 nm^2. This slight deviation is attributed by the very broad distribution of particle size, which can be visually perceived from the mask images shown in Fig. 3. Moreover, dimensions of the dispersed tactoids were obtained by extracting the line profiles of the mask images (Fig. 3). The lengths (or widths) are believed to be the width of the peak, obtained from the "findpeak" function in Matlab. For estimation convenience, each individual tactoid is assumed to have a rectangular shape, and the average size of each composite sample is assumed to be the multiple of width W and length L. Hence, the aspect ratio AR, where $AR = L/W$, ranges from 2 to 3. This is in agreement with the visual estimation in the magnified mask image (Fig. 3d) and Halpin-Tsai (HT) model fitting based on the strengthening effect of clay on thin film mechanical properties.
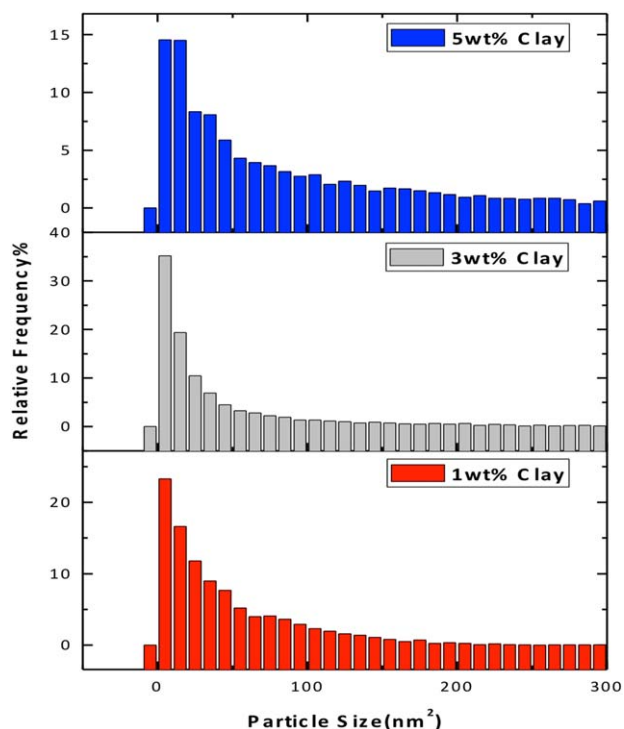

FIG. 2. Typical particle size distribution of PCL/Natural clay samples through digital analysis of TEM images. Results are obtained through counting frequency analysis with a bin size of 10, giving an average size of 40–80 nm^2, as summarized in Table 1. [Color figure can be viewed at wileyonlinelibrary.com].

Figure 4 depicts the level of dispersion further analyzed with Grazing Incidence Wide Angle X-ray Scattering (GIWAXS) (4a and 4b) and wide angle X-ray scattering (WAXS) (4c). The former is a proven technique for thin film analysis, whereas the latter is used to characterize natural clay in the powder form and free standing films. Figure 4c shows the scattering pattern of the Na+ Montmorillonite and free standing films. The d_{001} characteristic peak suggests a gallery spacing ≈1.18 nm according to Bragg's diffraction law $d_{001} = 2\pi/q$, consistent with the product information sheet, where $q = 4\pi(\sin\theta)/\lambda$ is the scattering vector with 2θ the scattering angle and λ the wavelength. With the absence of organic coupling agent, the inter-gallery spacing is smaller than commercialized organoclay, with interlayer distance ≈1.8 to 1.9 nm. The peak corresponding to the original basal spacing of 1.18 nm, based on WAXS, also occurs in the z profile of grazing incidence wide angle X-ray scattering for all the thin film composite samples, indicating a small amount of aggregation in the direction parallel to the silicon substrate. The small difference in q value between WAXS and GIWAXS is due to minor variation in X-ray wavelength, but they all correspond to the same d_{001} spacing. The presence of an additional peak at a smaller scattering angle ($q = 0.24$ $Å^{-1}$) in the out-of-plane direction (Fig. 4b) manifests the occurrence of intercalated nanostructure with an enlarged interlayer distance of 2.62 nm. The characterization peaks shown in the z profile are pointed by arrows in Fig. 4b. Furthermore, the scattering peaks revealing the dispersion morphology are much weaker and broader in the q_y profile (Fig. 4a) compared to q_z profile (Fig. 4b), meaning the forces during the flow coating (shear) and film drying process (surface tension) is inclined to align the clay sheets parallel to the substrate direction. This phenomenon has been observed previously in the same polymer filled with Cloisite 30B organoclay [39]. The absence of characteristic peaks in the q_y plane indicates that the clay tactoids are not vertically oriented within the film plane. Rather, they are horizontally oriented as confirmed by the peaks when the film is probed in the q_z direction. This is clearly a consequence of initial state of ordering/orientation of the large tactoids from the flow coating process. We anticipate in-plane enhancements of the film modulus because of the horizontal orientation of the tactoids as confirmed by GIWAXS measurements. To this, we performed SIEBIMM measurements as addressed in later sections. Figure 4c shows the WAXS pattern of free standing thick film samples. Peaks reflecting the intercalated tactoids in these free-standing thick films are more intensive than the thin film samples, which is likely inherent to the slow solvent evaporation process, which in turn, produces less homogeneous dispersion and larger intercalated clusters. This effect becomes more prominent at higher clay contents, as evidenced by more intensive and narrower d_{001} peaks with increasing clay loading. Peaks reflecting the original basal spacing of the natural clay are not observed in the free standing thick films during the drop cast and drying process by natural convection due to the absence of shear force applied in a preferential direction.

Figure 5 compiles the temperature-heat flow curve of nanocomposite samples. The presence of natural clay suppresses thermal stress relaxation, causing the neat PCL sample to have a broader but shorter melting peak compared to the clay-filled samples. Nevertheless, the area under the curve calculated through
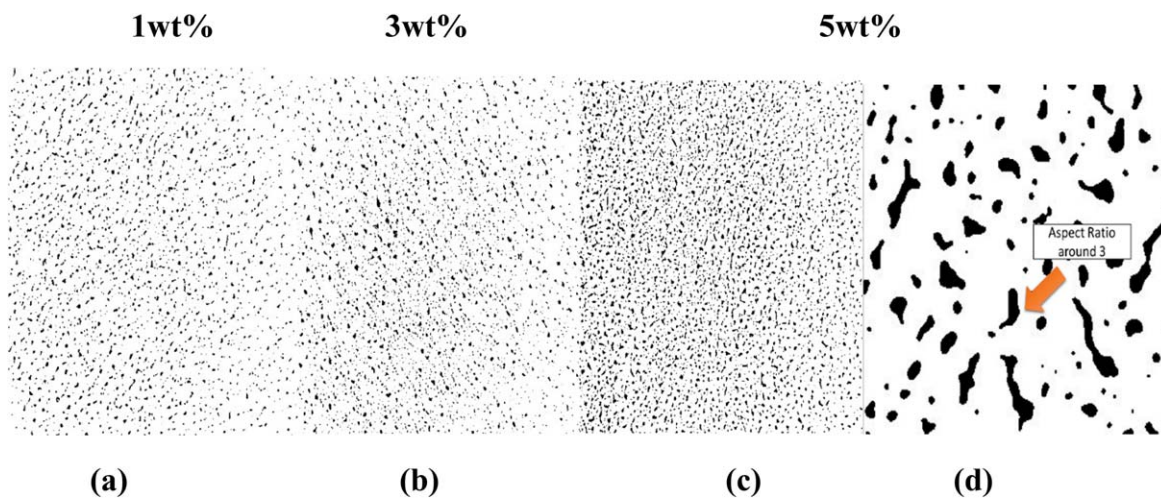
1wt%   **3wt%**   **5wt%**

(a)   **(b)**   **(c)**   **(d)**

FIG. 3. Color threshold treated TEM images for (a) PCL + 1% mass fraction clay, (b) PCL + 3% mass fraction clay, (c) PCL + 5% mass fraction, and (d) the magnified version of 5% mass fraction sample showing that the aspect ratio observed visually is in agreement with digital analysis. The area fraction is shown to increase with increasing clay content. [Color figure can be viewed at wileyonlinelibrary.com].

TA Universal Analysis software suggests that samples have a consistent mass fraction crystallinity of ≈50% with different clay loadings, based on a 100% crystalline enthalpy reference of 17.9 kJ/mol [52]. This result is consistent with previously studied PCL/Cloisite 30B systems, showing that the well-dispersed organoclay in the matrix does not change the degree of crystallinity, and mechanical enhancement is due to the intercalated nanostructures [39]. The consistency in crystallinity demonstrated in the current work allows further studies of segmental relaxation affected by the addition of nano-fillers rather than complications due to varying crystallinity.

Mechanical properties were investigated using the SIEBIMM technique, in which a submicron thin film is transferred onto a pre or post-stretched elastomer substrate (PDMS) and released, resulting in buckling due to a mismatch of Poisson's ratio between the film and elastomer substrate. Figures 6a–d compile the buckling images of the nanocomposite samples. In these images, the periodic buckling pattern is produced by deforming (post-stretched) the elastomer substrate. In this method, the Young's modulus of the film needs to be at least an order of magnitude higher than that of the elastomer substrate for good results [32]. Polycaprolactone is a semicrystalline polymer with a glass transition temperature, $T_g \sim 213K$ and a crystallinity of around 50%. The crystalline domains exhibit rigid, solid-like mechanical properties, and the amorphous domain behave as an elastomer due to its low. Therefore, the semi-crystalline domains serves as the main driving force for buckling, while the amorphous domains suppress buckling, resulting in a bimodal inhomogeneity in buckling pattern, useful to interpret film morphology. This phenomenon is indicated in the neat-PCL film (Figure 6a), wherein buckling occurs mostly inside the black regions (Region A), while the white regions exhibit significantly fewer buckling patterns (Region B). Hence, Region A is interpreted as incorporating crystalline-PCL rich regions and is buckling enhancing, whereas Region B incorporates amorphous-PCL regions and is buckling suppressing. As we increase the filler content, the size of each individual buckling-deficient region also increases, as shown in Figures 6b–d. Apparently, the

natural clay tactoids, having weak hydrogen bonding with the polymer backbone, are well-dispersed in the more flexible amorphous domains rather than in the rigid crystalline domains. The tail-to-tail-like clusters in the matrix likely interconnect different parts of amorphous regions, while simultaneously breaking apart the crystalline PCL regions across the film and, therefore, reducing the average size of the black regions. Figure 7 summarizes the relationship between clay loading and the average size of crystalline Region A, obtained by digitizing several different buckling images at each clay concentration. The error bar displays the standard deviation of buckling-region size among different images. The neat PCL has the largest error bar, because Region A forms a network across the entire film, causing large variation in its size as determined via this approach. In contrast, from 1% to 5% mass fractions, Region B regimes start to break apart Region A regimes, making the size of each buckling-rich site more uniform, manifested in a significantly smaller standard deviation. Furthermore, it also shows that the average size of the crystalline Region A decreases as we increase the filler loading from 0% to 5% mass fraction. Further, although the average crystallite size has a decreasing trend shown in Figure 7, the area fraction stays around 45%–60%. Hence, although Region A covers crystalline-rich regimes as per our prediction, these regions are not entirely crystalline domain because its area fraction is not exactly 50% on every buckling image. The overall trend fluctuates around 50%, consistent with DSC results showing 50% crystallinity, as discussed previously. Therefore, we assume the dispersed natural clay tactoids only change the arrangement of the crystalline regions across the film, but not the overall crystallinity. Such a rearrangement is not evident in previous studies on PCL-organoclay composites, because the strong interaction between the backbone and the surfactant enables particles to be well-dispersed in both crystalline and amorphous domains [39, 54]. In such cases, the organoclay systems exhibit uniform buckling patterns of organoclay-filled composites across the entire film, allowing Fast Fourier Transform (FFT) analysis on the wavelength. Unlike such organoclay systems, the rearrangement of the buckling and non-buckling
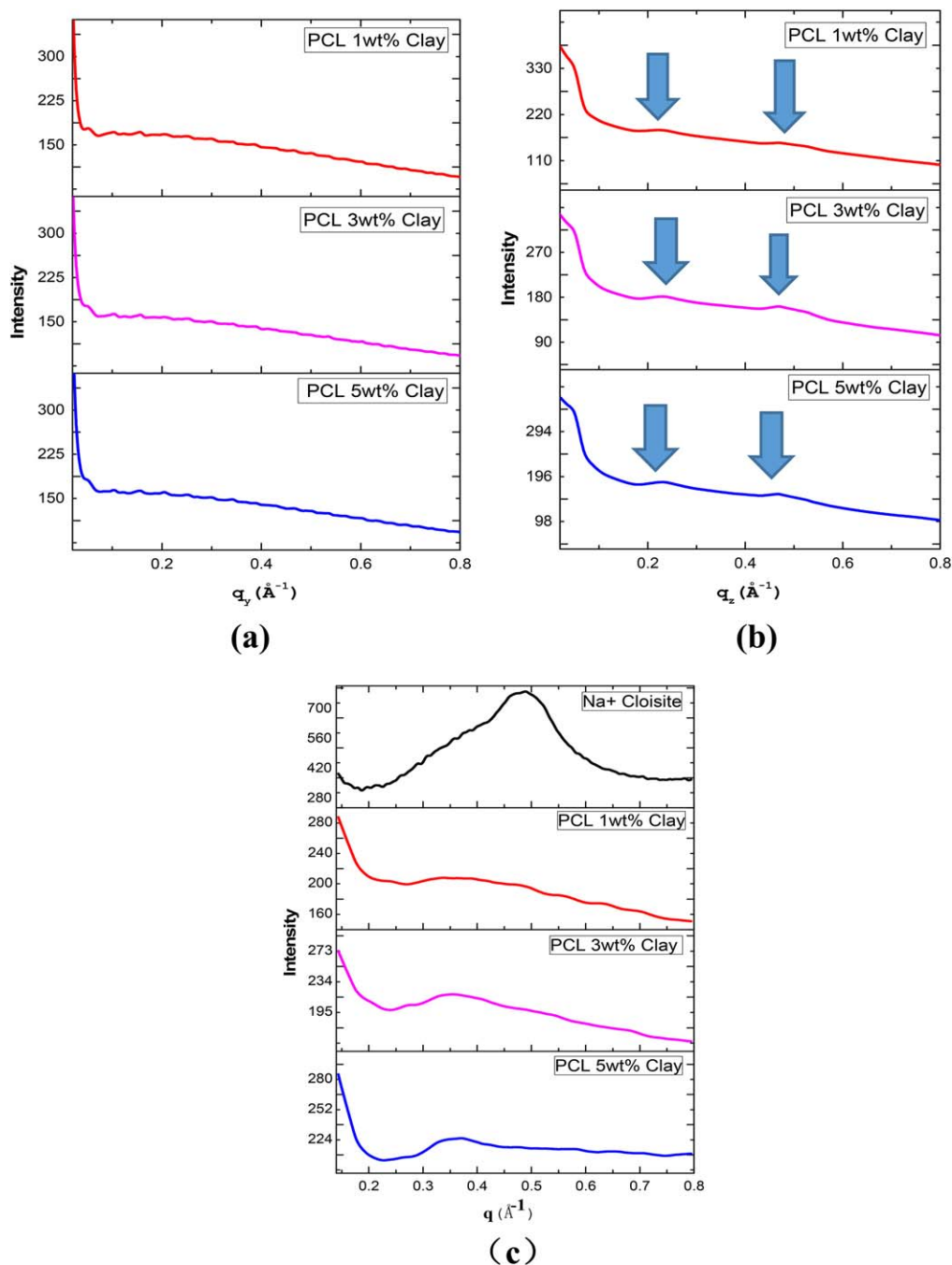
FIG. 4. a) Line Profiles of grazing incidence wide angle scattering of ultrathin films in the (a) in-plane(y profile) and (b) out-of-plane (z-profile) directions. All the measurements were performed above the critical scattering angle. (c) Wide angle X-ray scattering patterns of free-standing thick films. Low intensity peaks corresponding to d_{001} is at $q = 0.37$ Å^{-1}, meaning the majority of the clay sheets are spread out in the polymer matrix with a small amount of intercalated nanostructures. With higher clay concentrations, intercalated peaks have slightly higher intensities, indicating the existence of more intensive intercalated clusters. [Color figure can be viewed at wileyonlinelibrary.com].

regions in this study makes it difficult to perform FFT analysis. Hence, the wavelength was calculated by taking the average wavelength of different regions (both Region A and Region B), resulting in uncertainties of around 40 Mpa. The average Young's modulus goes from 182 Mpa to 211 Mpa. TEM analysis suggests clay tactoids have aspect ratios around 2-2.4. Based on the Halpin-Tsai (HT) Model's prediction [53], these aspect ratio values can give rise to a nominal 1.08% increase in Young's modulus. Our results are in rough agreement with this prediction. The absence of noticeable modulus increase is mainly attributable to two factors. First, the aspect ratio of clay tactoids is low. The continuum-filler effect predicted by the HT model is within the error range. Second, the natural clay tactoids prefer to remain in the amorphous phase, while buckling is
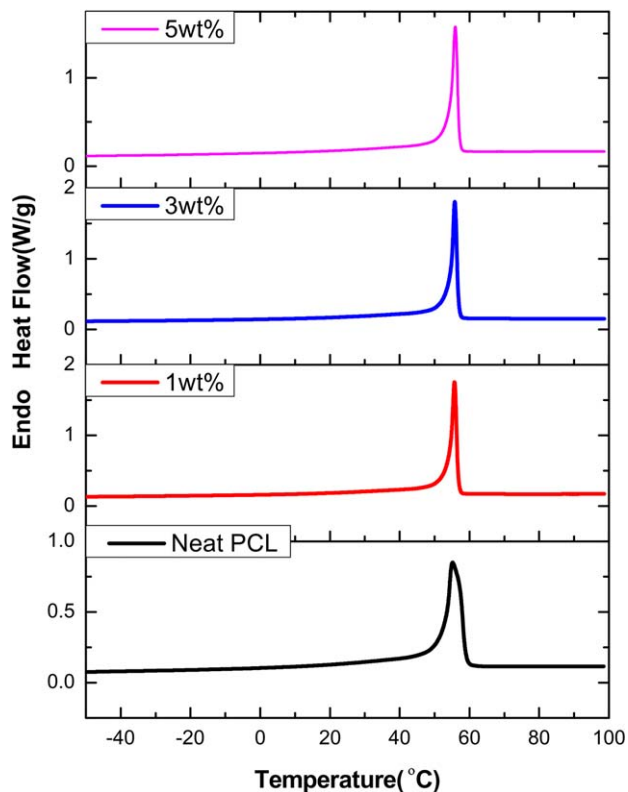
FIG. 5. Typical heat flow-temperature curves of PCL/natural clay samples on cooling, with endotherm direction being down. [Color figure can be viewed at wileyonlinelibrary.com].

mainly reinforced in the crystalline phase. In other words, this system is already self-reinforced by the crystalline domains; introducing reinforcing particles to the amorphous rubbery domains does not have a large effect on mean modulus. We note that this outcome could very well be different if the test temperature were below the T_g of the amorphous regions.

Figure 8 depicts the overall dielectric relaxation patterns of free standing thick samples with the addition of different amount of clay particles at 10 Hz, where all three types of relaxation regimes, namely α relaxation in the super-cooled temperature regime, β relaxation in glassy state, and normal mode relaxation at higher temperatures, have been observed. The peak occurring at low temperature region (from $-150°C$ to $-75°C$) is the sign of β relaxation, whereas the α relaxation is manifested by the peak around $-50°C$. (As observed here and shown elsewhere [54], whereas PCL has a rigid amorphous phase [54], it does not display a separate process related to confined amorphous material, such as has been observed in polyisoprene [59].) Above $-25°C$, the system starts to undergo normal mode relaxation, where the point of discontinuity around $50°C$ is a manifestation of crystallization temperature, consistent with the temperature at which DSC heat flow exhibits a crystalline peak. The majority of the relaxation behaviors described above are in agreement of relevant studies of PCL/ Cloisite 30B nanocomposites [49]. The only exception is that Cloisite 30B surfactant allows more molecular chains to diffuse into the galleries to cause an increased melt viscosity and thus changes in terminal relaxation time during normal mode relaxation. On the other hand, natural clay, having much
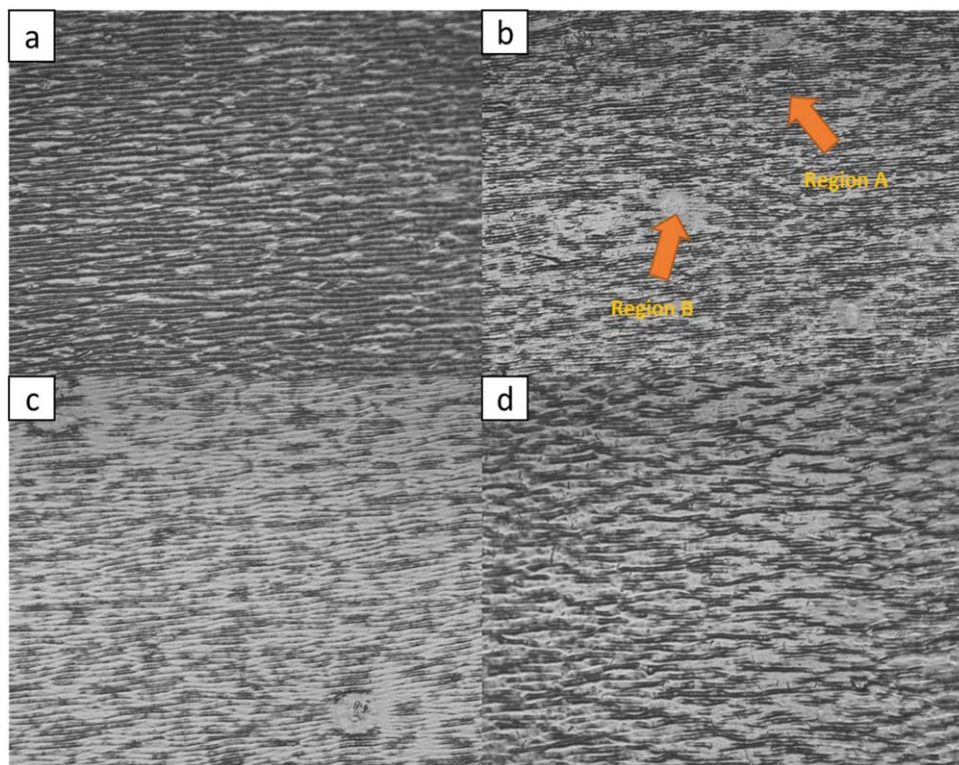

FIG. 6. Buckling patterns of composite films with filler loadings of a) 0wt% mass fraction, b) 1wt% mass fraction, c) 3wt% mass fraction, and d) 5wt% mass fraction. [Color figure can be viewed at wileyonlinelibrary.com].
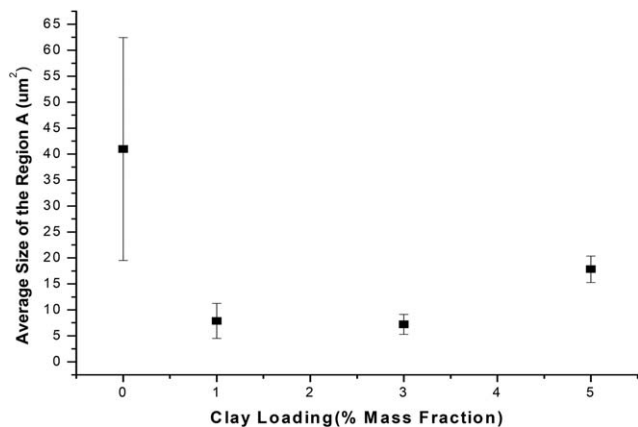
FIG. 7. The relationship between clay loading and the average size of the buckling regions.

FIG. 8. Dielectric loss (ε'') versus temperature curve of free standing films. The curve depicts the overall dielectric relaxation behaviors of samples with different natural clay loadings at 10 Hz. [Color figure can be viewed at wileyonlinelibrary.com].

weaker interaction with the polymer matrix, does not tailor the behaviors of normal mode relaxation at this particular frequency. A secondary relaxation behavior, the β relaxation, was observed in both neat PCL and nanocomposites, and a Havriliak-Negami function was applied to fit the isothermal dielectric loss data (ε'') at low temperature range [60].

$$\varepsilon^* = \varepsilon' - i\varepsilon'' = \varepsilon_s + \frac{\Delta\varepsilon}{[1 + (i\omega\tau_{HN})^n]^m} \quad (2)$$

Here, $\Delta\varepsilon$ is the dielectric strength, which is the difference between the static ε_s and instantaneous ε_i dielectric constants. τ_{HN} is the Havriliak-Negami relaxation time, n and m are shape parameters. The experimental relaxation time τ (different from the fit parameter τ_{HN}) was determined from the fitting parameters, following Eqs. 3 and 4

$$\tau = \frac{1}{2\pi f_{max}} \quad (3)$$

$$f_{max} = \frac{1}{2\pi\tau_{HN}} \left[\frac{\sin\left(\frac{\pi m}{2+2m}\right)}{\sin\left(\frac{\pi n m}{2+2m}\right)} \right]^{1/n} \quad (4)$$

where f_{max} corresponds to the frequency of the experimental dielectric loss peak maximum.

The temperature dependence of the beta relaxation time is shown in Fig. 9. Both neat PCL and the nanocomposite display an Arrhenius temperature dependence and the data sets appear to overlap each other. That is to say, the weak interaction between PCL host matrix and natural clay does not affect the slow β process. The unchanged activation energy was also observed in PCL/Cloisite 30B systems, having stronger interactions.

$$\tau = \tau_0 \exp\left(\frac{B}{T - T_0}\right) \quad (5)$$

Segmental relaxation times (α relaxation) and their reciprocal temperature data were obtained through locating the temperature corresponding to α peak for a series of frequencies and fitted with Vogel-Fulcher-Tammann model, following the expression of Eq. 5, where τ (α relaxation time) and T (temperature) are variables for the curve fit, while τ_0, B and T_0 are VFT constants to be solved. Through model fitting, the extrapolated values of
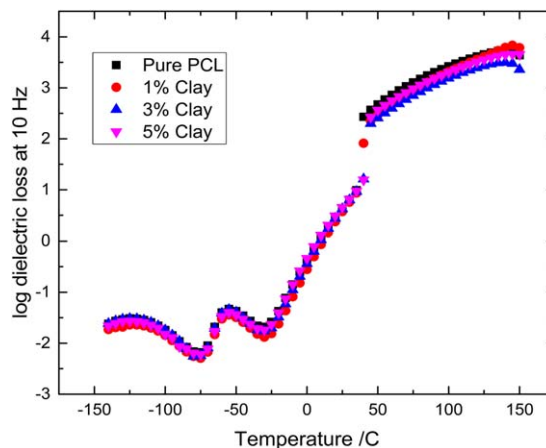
temperature corresponding to the relaxation time at $\tau = 100$ s define the glass transition temperature (T_g). Fragility is obtained through T_g and fitted VFT parameters according to definition and the algebraically equivalent form based on the VFT model (Eq. 5) [54, 55], where m is the fragility index, B and T_0 are the same VFT parameters in Eq. 5.

$$m = \left(\frac{\partial \log(\tau_\alpha)}{\partial T_g/T}\right)_{T=T_g} = \frac{BT_g}{(T_g - T_0)^2 [\ln(10)]} \quad (6)$$

In the case of PCL/natural clay systems, VFT parameter B and T_0 are ≈ 850 K and ≈ 189 K, respectively, which are consistent with the earlier study for the PCL/organoclay systems. Composite samples with all the filler concentration exhibit a uniform $T_g \approx 213$ K based on VFT extrapolation. The kinetic fragility index remains unaffected around 142. Possible explanation for the intact T_g and fragility might be the low volume fraction for the clay content due to the low density of
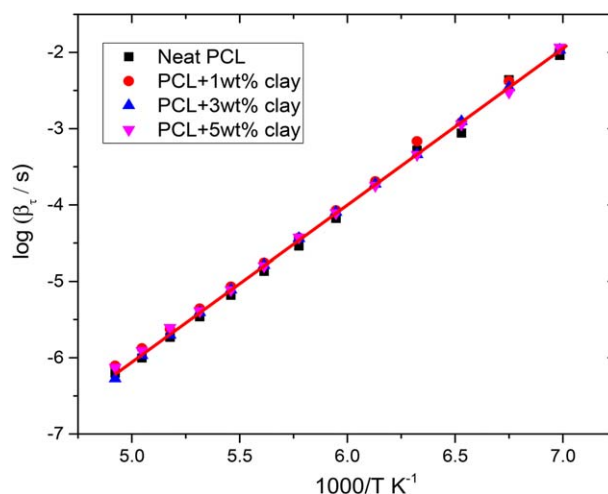

FIG. 9. Segmental relaxation behaviors of free standing films as interpreted by the temperature dependence of the slow β relaxation time β_τ. [Color figure can be viewed at wileyonlinelibrary.com].

Montmorillonite in addition to fact that the tactoid-like clay clusters are not accessible to the polymer matrix in a molecular level. This is consistent with the previous results showing that the intercalated organoclay does not tailor segmental dynamics based on the unchanged VFT parameters [54]. In our study, the dielectric properties are not affected for two reasons. First, because of the lack of strong intercalation-induced confinement of polymer chains, the chains are not likely to be strongly confined by the particles. Even though there are indications that natural clay tactoids prefer to remain in the amorphous phase, the existing confinement effect of the crystalline phase also may render negligible any additional confinement imposed by the nanoparticles the effect of nanoparticles negligible. Finally, the interactions between polymer matrix and clay particles are fairly weak (a consequence of the surfactant-free approach), such that this system may be in the vicinity of the compensation point in interfacial energy discussed above, at which bulk-like dynamics are recovered [51].

CONCLUSIONS

A novel approach combining water-assisted compounding and Mackay's strategy of nanoparticle dispersion is shown to be an effective method to disperse surfactant-free clay in PCL host matrix, despite the absence of strong polymer-clay interactions. Ultrathin films and freestanding thick films were prepared through flow coating and drop casting. Detailed dispersion morphologies have been investigated through the digitization of TEM images and corroborated by WAXS and GIWAXS. Mechanical properties, characterized by SIEBIMM, suggest that natural clay-filled tactoids prefer to remain in the more flexible amorphous phase and tend to break down the crystalline-rich regimes across the film. The low aspect ratio values and lack of intercalation in the buckling-rich regimes result in insignificant changes in Young's modulus. Our samples exhibit similar dynamic behaviors during glass transition to those observed in PCL-organoclay systems, suggesting the presence of the crystalline phase has a more significant impact and dynamics and mechanics than does nanoparticle confinement.

REFERENCES

1. A. Okada, and A. Usuki, *Macromol. Mater. Eng.*, **291**, 1449 (2006).

2. N.N. Bhiwankar, and R.A. Weiss, *Polymer*, **46**, 7246 (2005).

3. N.N. Bhiwankar, and R.A. Weiss, *Polymer*, **47**, 6684 (2006).

4. B.F. Ports, and R.A. Weiss, *Ind. Eng. Chem. Re.*, **49**, 11896 (2010).

5. H.-M. Park, X. Liang, A.K. Mohanty, M. Misra, and L.T. Drzal, *Macromolecules*, **37**, 9076 (2004).

6. J.M. Hwu, G.J. Jiang, Z.M. Gao, W. Xie, and W.P. Pan, *J. Appl. Polym. Sci.*, **83**, 1702 (2002).

7. Y. Liang, Y. Wang, Y. Wu, Y. Lu, H. Zhang, and L. Zhang, *Polym. Test.*, **24**, 12 (2005).

8. R.A. Vaia, and E.P. Giannelis, *Macromolecules*, **30**, 8000 (1997).

9. C. Zeng, and L. Lee, *J. Macromol.*, **34**, 4098 (2001).

10. S.-G. Kim, E.A. Lofgren, and S.A. Jabarin, *Adv. Polym. Technol.*, **32**, (2013).

11. M. Jahangiri, S.H. Jafari, H.A. Khonakdar, M. Tarameshlou, and I.F. Ahmadi, *J. Vinyl Add. Technol.*, **21**, 70 (2015).

12. S.-Y.A. Shin, L.C. Simon, J.B.P. Soares, and G. Scholz, *Polymer*, **44**, 5317 (2003).

13. M. Salehi, and M. Razzaghi-Kashani, *J. Appl. Polym. Sci.*, **126**, 253 (2012).

14. Y.-P. Wu, Y.-Q. Wang, H.-F. Zhang, Y.-Z. Wang, D.-S. Yu, L.-Q. Zhang, and J. Yang, *Composit. Sci. Technol.*, **65**, 1195 (2005).

15. W.F. Bixby, Google Patents (1950).

16. A. Zhuk, R. Mirza, and S. Sukhishvili, *ACS Nano*, **5**, 8790 (2011).

17. Y.-H. Yang, F.A. Malek, and J.C. Grunlan, *Ind. Eng. Chem. Res.*, **49**, 8501 (2010).

18. J. Hickey, N.A.D. Burke, and H.D.H. Stöver, *J. Membr. Sci.*, **369**, 68 (2011).

19. D.W. Kim, J. Kumar, and A. Blumstein, *Appl. Clay Sci.*, **30**, 134 (2005).

20. M.E. Mackay, A. Tuteja, P.M. Duxbury, C.J. Hawker, B. Van Horn, Z. Guan, G. Chen, and R.S. Krishnan, *Science*, **311**, 1740 (2006).

21. S. M. King, in *Modern Techniques for Polymer Characterization*, R. A. Pethrick, J. V. Dawkins, Eds. Wiley, New York (1999).

22. J. S. Higgins, H. C. Benoît, *Polymers and Neutron Scattering*, Clarendon Press, Oxford (2002), p. 436.

23. A. Tuteja, M.E. Mackay, S. Narayanan, S. Asokan, and M.S. Wong, *Nano Lett.*, **7**, 1276 (2007).

24. A. Tuteja, P.M. Duxbury, and M.E. Mackay, *Macromolecules*, **40**, 9427 (2007).

25. G. Lagaly, and S. Ziesmer, *Adv. Colloid Interf. Sci.*, **100–102**, 105 (2003).

26. Z.-Z. Yu, G.-H. Hu, J. Varlet, A. Dasari, and Y.-W. Mai, *J. Polym. Sci. B Polym. Phys.*, **43**, 1100 (2005).

27. K.E. Strawhecker, and E. Manias, *Chem. Mater.*, **12**, 2943 (2000).

28. G. Stoclet, M. Sclavons, and J. Devaux, *J. Appl. Polym. Sci.*, **127**, 4809 (2013).

29. V.P. Cyras, L.B. Manfredi, M.-T. Ton-That, and A. Vázquez, *Carbohydrate Polym.*, **73**, 55 (2008).

30. C.M. Stafford, K.E. Roskov, T.H. Epps, and M. Fasolka, *J. Rev. Sci. Instrum.*, **77**, 023908 (2006).

31. R. Zhang, G. Singh, A. Dang, L. Dai, M.R. Bockstaller, B. Akgun, S. Satija, and A. Karim, *Macromol. Rapid Commun.*, **34**, 1642 (2013).

32. C.M. Stafford, C. Harrison, K.L. Beers, A. Karim, E.J. Amis, M.R. VanLandingham, H.-C. Kim, W. Volksen, R.D. Miller, and E.E. Simonyi, *Nat. Mater.*, **3**, 545 (2004).

33. C.M. Stafford, S. Guo, C. Harrison, and M.Y.M. Chiang, *Rev. Sci. Instrum.*, **76**, 062207 (2005).

34. D. Tahk, H.H. Lee, and D.-Y. Khang, *Macromolecules*, **42**, 7079 (2009).

35. E.A. Wilder, S. Guo, S. Lin-Gibson, M.J. Fasolka, and C.M. Stafford, *Macromolecules*, **39**, 4138 (2006).

36. J.E. Longley, and M.K. Chaudhury, *Macromolecules*, **43**, 6800 (2010).

37. E.D. Cranston, M. Eita, E. Johansson, J. Netrval, M. Salajková, H. Arwin, and L. Wågberg, *Biomacromolecules*, **12**, 961 (2011).

38. A.J. Nolte, R.E. Cohen, and M.F. Rubner, *Macromolecules*, **39**, 4841 (2006).

39. H. Yuan, G. Singh, D. Raghavan, A.M. Al-Enizi, A. Elzatahry, and A. Karim, *ACS Appl. Mater. Interf.*, **6**, 13378 (2014).

40. A. Bansal, H. Yang, C. Li, K. Cho, B.C. Benicewicz, S.K. Kumar, L.S. Schadler, *Nat. Mater.*, **4**, 693 (2005).

41. D.S. Simmons, *Macromolecular Chem. Physic.*, **217**, 137 (2016).

42. M.D. Ediger, *Ann. Rev. Physic. Chem.*, **51**, 99 (2000).

43. Ranko, R. *Journ. Physic: Condensed Matter.*, **14**, R703 (2002).

44. C. Donati, S.C. Glotzer, P.H. Poole, W. Kob, and S.J. Plimpton, *Physi. Rev. E.*, **60**, 3107 (1999).

45. K.W. Stöckelhuber, A. Das, R. Jurk, and G. Heinrich, *Polym.*, **51**, 1954 (2010).

46. S. Kim, and J.M. Torkelson, *Macromolecules*, **44**, 4546 (2011).

47. S. Napolitano, A. Pilleri, P. Rolla, and M. Wübbenhorst, *ACS Nano*, **4**, 841 (2010).

48. C.B. Roth, and J.M. Torkelson, *Macromolecules*, **40**, 3328 (2007).

49. C.J. Ellison, and J.M. Torkelson, *Nat. Mater.*, **2**, 695 (2003).

50. R.J. Lang, W.L. Merling, and D.S. Simmons, *ACS Macro Lett.*, **3**, 758 (2014).

51. W.L. Merling, J.B. Mileski, J.F. Douglas, and D.S. Simmons, *Macromolecules*, **49**, 7597 (2016).

52. B. Wunderlich, *Progress Polym. Sci.*, **28**, 383 (2003).

53. J. Lee, J.H. Mangalara, and D.S. Simmons, *Jour. Poly. Sci. Part B: Poly. Phys.*, **55**, 907 (2017).

54. K.A. Masser, H. Yuan, A. Karim, and C.R. Snyder, *Macromolecules*, **46**, 2235 (2013).

55. Certain commercial equipment, instruments, or materials are identified in this paper in order to specify the experimental procedure accurately. Such identification is not intended to imply recommendation or endorsement by the National Institute of Standards and Technology, nor is it intended to imply that the materials or equipment identified are necessarily the best available for the purpose.

56. B. Wunderlich, *Thermal Analysis of Polymeric Materials* (Springer, New York, 2005), p. 785.

57. J.C.H. Affdl, and J.L. Kardos, *Poly. Eng. & Sci.*, **16**, 344 (1976).

58. B. Wunderlich, *Pro. Polym. Sci.*, **28**, 383 (2003).

59. S. Cerveny, P. Zinck, M. Terrier, S. Arrese-Igor, A. Alegría, and J. Colmenero, *Macromolecules*, **41**, 8669 (2008).

60. S. Havriliak, and S. Negami, *Polym.*, **8**, 161 (1967).

61. J. Rault, *Jour. Non-Crystall. Sol.*, **271**, 177 (2000).

62. K. Kunal, C.G. Robertson, S. Pawlus, S.F. Hahn, and A.P. Sokolov, *Macromolecules*, **41**, 7232 (2008).